Heliyon 9 (2023) e20585

Contents lists available at ScienceDirect

Heliyon

journal homepage: www.cell.com/heliyon

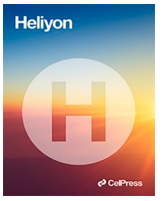

Predictive analysis of the power spectral irradiance from blackbody radiation source using single pixel detector

Hui Jing Lee [a,*], Pin Jern Ker [b], Mansur Mohammed Ali Gamel [c], Md Zaini Jamaludin [a], Yew Hoong Wong [d]

[a] *Electrical & Electronics Department, College of Engineering, Institute of Power Engineering, Universiti Tenaga Nasional, 43000, Kajang, Selangor, Malaysia*
[b] *Electrical & Electronics Department, College of Engineering, Institute of Sustainable Energy, Universiti Tenaga Nasional, 43000, Kajang, Selangor, Malaysia*
[c] *Electronic Engineering Department, Universitat Politècnica de Catalunya, Barcelona, 08034, Spain*
[d] *Department of Mechanical Engineering, Faculty of Engineering, Universiti Malaya, 50603, Kuala Lumpur, Malaysia*

ARTICLE INFO

Keywords:
Spectral irradiance
Power densities
Radiation temperature
Energy

ABSTRACT

Accurate spectral irradiance measurement in the near-infrared range is significant for the design and characterization of photodetector and photovoltaic cells. Approximation method is commonly used to solve for the input power using estimated spectral irradiance, where the dependency on wavelength and temperature remains uncertain. This study aims to determine the power spectrum at different radiation temperatures using a single pixel photodetector, taking into consideration factors such as transmission spectra of alumina radiator, CaF_2 collimating lens, responsivity, and measured photocurrent information of photodetectors. Utilizing predictive mathematical model, five commercial photodetectors, including Silicon, Germanium, $In_{0.53}Ga_{0.47}As$, $In_{0.73}Ga_{0.27}As$, and $In_{0.83}Ga_{0.17}As$ were used to solve for the power densities as a function of wavelengths at radiation temperatures of 1000 °C and 1500 °C. The spectral irradiance of photodetectors was determined with a percentage difference of <4.9 %, presenting an accurate power density estimation for the spectrum at a wide range of radiation temperatures. Power irradiance data obtained were validated in the narrow wavelength range with 1000 nm, 1400 nm, 1500 nm, and 2000 nm bandpass filters. The reported work demonstrates a simple and efficient way which could contribute to develop a cost-effective method of measuring and determining the spectrum irradiances of objects at different radiation temperatures. This predictive analysis method hopefully intensifies the progress of efforts to reduce the reliance on complex optoelectronic instruments in accurately solving power irradiance information.

1. Introduction

Blackbody source is commonly used as a primary tool in optical radiation measurement. Accurate spectral irradiance information is required for various fields such as the spectral irradiance measurement in solar cell [1], remote sensing [2] and climate change monitoring [3]. In particular, the blackbody spectral irradiance information receives great attention in the photovoltaic (PV) and thermophotovoltaic (TPV) technology analysis [4]. The accuracy of power intensity information is also crucial to investigate the

* Corresponding author.
E-mail address: LHJing@uniten.edu.my (H.J. Lee).

https://doi.org/10.1016/j.heliyon.2023.e20585
Received 19 June 2023; Received in revised form 11 August 2023; Accepted 29 September 2023
Available online 5 October 2023

photo-response dependence in photodetector application [5]. For example, recent research highlighted the feasibility of organic photodiode for high-speed photodetector application, in which the spectral irradiance information correspond to the wavelength need to be carefully analysed [6]. In general, the variation in spectral irradiance has demonstrated a strong dependence on wavelength information and temperature condition [7]. Based on Plank's law of blackbody radiation and Wien's displacement law, the sensitivity of the spectral irradiance information increases in the short wavelength region with respect to the change in temperature [8]. For power density measurement, spectrum analysers such as UV-biometer (280 nm–400 nm) [9], pyranometer (200–2800 nm) [10], and multiwavelength sun photometer (340–1640 nm) [11] are commonly used for short wavelength region <3000 nm spectrum measurement. Studies show that pyrheliometer (up to 4000 nm) [12], thermopile (3000–5000 nm), and spectrometer (2000 nm–9000 nm) [13] are tools for spectrum measurement in the mid-wavelength region 3000 nm–8000 nm. In addition, analysers such as pyrgeometer (up to 42 000 nm) [10,14] and interferometer are used for the long-wavelength region (>8000 nm) [15]. These tools are essential to assist in power density measurement for the application of accurate photovoltaic design and high speed photodetectors research [5, 16].

Focusing on the short wavelength region <3000 nm, pyroelectric radiometer is also commonly used to solve for spectral irradiance in the visible to mid-infrared range. For example, Rs-5900 pyroelectric radiometer is able to measure 5 μW −100 mW of power range in the wavelength range of (250 nm–3000 nm) up to ±1 % accuracy [17]. This device is often used to calibrate laser power meter [18], blackbody emitters [19], and UV exposure meter [20]. On the other hand, spectrometer is commonly used to measure the power density spectrum of devices owing to its high accuracy advantage, but annual spectral calibration down to 1 nm wavelength is reported to be essential to guarantee the accuracy of measurement output [21]. To further improve the spectrometer accuracy, spectrometer is incorporated with cosine correction for the cosine error inherent based on Lambert's cosine law [16,22]. In addition, the grating performance selection factors such as thickness of grating, spectral resolution, groove density and efficiency of grating materials are important to maximize the efficiency in spectroscopy for their well-suited applications [23,24]. For example, the feasibility of Si, Gallium Nitride (GaN), Indium Gallium Arsenide (InGaAs) and Indium Phosphide (InP) grating materials were evaluated for Ultraviolet–visible (UV–Vis) spectrometer (200–700 nm) in COVID-19 vaccine research application, where InGaAs is reported to produce the highest efficiency at 87.45 % [24]. Nevertheless, spectrometers in the short-wave infrared (SWIR) region (900–2600 nm) using InGaAs detectors are suitable for high-speed long wavelength photodetectors study. However, they are often more costly compared to Silicon-based detectors due to the gap in technology maturity [25]. In such case, costing of SWIR spectrometers appears to be a major concern, where recent work highlighted the feasibility of a novel low cost SWIR spectrometer development, with the integration of multivariate data analysis for archaeological application [26].

Research efforts towards studying the power density of TPV cells based on the materials' cut-off wavelength and blackbody temperature have increased in the recent years [27]. It is also of researchers' interest to study the effect of blackbody temperature and illumination intensities on the TPV cell performance [4,28]. Efforts were driven to optimize the semiconductor devices cell structure in the motivation to decrease the electrical and optical losses for TPV application. To achieve this aim, the characterization process of the TPV cell appears to be crucial. In such case, the blackbody emitter power landing on the device must be carefully determined with minimal error to accurately solve and understand the cell performance behaviour. Previous work by Tervo et al. [8] calorimetrically measured for power density and heat lost dissipation of the 0.74 eV InGaAs TPV cell. The measurement method was compared with simulation data, where the simulation data was reported to over predict the cell efficiency at the low range of temperature (1100–1700 °C), possibly due to the heat loss in the measurement setup [8]. In the recent work reported by Ester et al. [29], the electrical power of the 0.74 eV InGaAs device under 1592 °C emitter is measured using the 4-wire method, while the dissipated heat is measured using the calorimeter. The probe contact must be carefully controlled under room temperature during the measurement process to prevent heat leakage via the contact [29]. In the near field power density calculation by Luchessi et al. [30], range of deviation in the radiative power was taken into consideration using the proximity approximation (Derjaguin approximation). Despite there is reported work by Rousseau et al. [31] on near-field radiative transfer for Silica substrate (30–2500 nm) which agrees with the proximity approximation, inconsistency of proximity approximation with disagreement to the theoretical data was reported by Chen et al. [32].

Simulation wise, Mansur et al. [33] reported on multi-variable optimization for $In_{0.53}Ga_{0.47}As$ under 800–2000 K blackbody radiation using Silvaco software, where the input power density was calculated based on 50 % of beam illumination intensity assumption. In another study by Tan et al. [34], mathematical calculation with Planck's formula was used to solve for the expected cell input power, highlighting the limitation of an ideal power meter for the input power measurement. Iles et al. [35] approximated the input power density up to 10 % of the blackbody radiation above the cut-off wavelength to calculate the efficiency, a practical assumption when using selective optical filters in the measurement. To summarize, the input power on device is commonly solved with mathematical calculation, which appears to be more complex with assumption made on the loss of radiative power. Measurement wise, the input power is often estimated with range of deviation, where uncertainty in the influence of spectral irradiance dependency on wavelength and temperature are still poorly understood. Hence, an accurate radiative power solver is significant to give a better overview on the cell efficiency and performance with respect to the system design, in which the radiative power at different temperature should be indicated in a very accurate manner.

This study investigates the power spectrum irradiances using predictive mathematical model and analysis based on the measured photocurrent data of five commercial photodetectors: Si, Germanium (Ge), $In_{0.53}Ga_{0.47}As$, $In_{0.73}Ga_{0.27}As$, and $In_{0.83}Ga_{0.17}As$. With reference to the photocurrent measurement result, the power density information of photodetectors under temperature exposure of 1000 °C and 1500 °C are analysed and validated with bandpass filters across the wavelength spectrum. The temperatures of interest studied by this work are due to the practicality of waste heat recovery potential in the furnace system, power plant and steel industries [36,37], and they are relevant in establishing the workability of the proposed method since it is within the temperature range for many

practical applications. This work portrays the development of cost-effective method to determine the spectrum irradiances of high-temperature objects at varying temperatures using single pixel detector. The proposed method drives the efforts in lowering the reliance on complicated optoelectronic instruments to accurately solve for the power irradiance as a function of wavelength.

2. Experimental design and mathematical model

The experimental setup for the spectral irradiance's measurement is illustrated in Fig. 1. The initial setup to solve power spectral using single pixel detector comprises of the radiation oven (hereafter named as blackbody source) that acts as the high-temperature radiation source, aperture, and Calcium Fluoride (CaF_2) plano-convex lens. The CALsys-1700 blackbody source with Alumina ceramic radiator functions as the heat source which radiates power spectrum at temperatures of 500 °C up to 1700 °C.

In general, a blackbody perfectly absorbs and radiates wavelengths from all direction where the fundamental of operation obeys Lambert's law [38]. The physical phenomenon of an ideal blackbody thermal radiation is explained based on the fundamental of Planck's law, which expresses the boundary limit of energy emission or exchangeable by a particular object [39]. In this context, the spectral radiation intensity of a blackbody, $F(\lambda, T_{BB})$ with reference to the wavelength and temperature is derived as:

$$F(\lambda, T_{BB}) = \frac{2\pi hc^2}{\lambda^5\left(\exp\left(\frac{hc}{k_B \lambda T_{BB}}\right) - 1\right)} \tag{1}$$

where λ is the photons wavelength, Boltzmann constant, k_B is expressed as 1.380×10^{-23} J/K, c is the speed of light. In Eq. (1), T_{BB} is the blackbody temperature in the unit of K.

An aperture with 2 cm diameter controls the light beam's exposure, confining the emitted light source from the blackbody to the photodetector under test. CaF_2 plano-convex lens with a focal length of 15 cm is aligned with the aperture to collimate the light source before landing on the photodetectors. In addition, the optimum distance between the aperture and CaF_2 lens is taken at 10 cm, taking into account that there is a 5 cm gap between the Alumina radiator installed in the blackbody source from the opening of the blackbody. Five commercials photodetectors with different cut-off wavelengths are used to measure the power spectrum: Si (1060 nm), Ge (1600 nm), $In_{0.53}Ga_{0.47}As$ (1700 nm), $In_{0.73}Ga_{0.27}As$ (2100 nm), and $In_{0.83}Ga_{0.17}As$ (2600 nm). Table 1 lists the photodetectors area, cut-off wavelength and wavelength operation range of the five tested photodetectors. For the validation process of the power spectrum across wavelengths, the bandpass filter is positioned after the aperture to allow signal in the selected range of wavelength to pass through and land onto the photodetector. The data extracted is used for further detailed analysis of the signal information at a specific wavelength range to validate the power spectrum. Bandpass filters used in this study are in the range of 1000 bandpass filter (hereafter known as BP) (975–1025 nm), 1400 BP (1375–1425 nm), 1500 BP (1475–1525 nm), and 2000 BP (1975–2025 nm). The range of study for the photodetectors and bandpass filters maps across the near-infrared (NIR) wavelength region (400 nm–2600 nm), which would be made useful for semiconductor devices application in the NIR wavelength region.

The photocurrent information of photodetectors in Table 1 was measured at zero bias condition (no external voltage applied to the

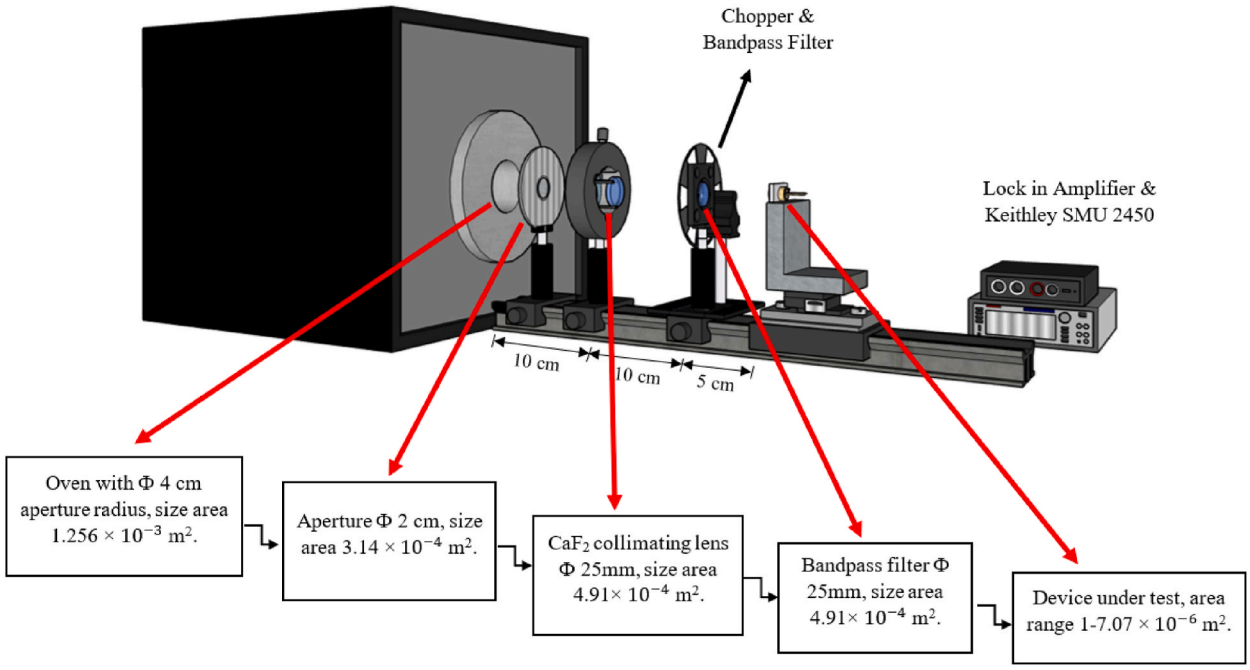

Fig. 1. Experimental setup for power density measurement and estimation of power irradiance ratio arriving at the device under test.

Table 1
Specifications of photodetectors as device under test.

Photodetector	Cut-off Wavelength (nm)	Device Area (m^2)	Detectable Wavelength Range (nm) from Device Specifications	Datasheet Ref
Si	1060	1×10^{-6}	400–1090	[40]
Ge	1600	7.07×10^{-6}	800–1800	[41]
$In_{0.53}Ga_{0.47}As$	1700	3.1×10^{-6}	800–1800	[42]
$In_{0.73}Ga_{0.27}As$	2100	3.14×10^{-6}	900–2160	[43]
$In_{0.83}Ga_{0.17}As$	2600	3.14×10^{-6}	900–2600	[44]

photodetector) with the source measure unit (Keithley SMU 2450) and the lock-in amplifier, which was then used to calculate the photocurrent density information based on the device area. Next, the Boston Electronics digital dual-phase lock-in amplifier and phase-locked chopper in Fig. 1 were used to perform signal acquisition, digital demodulation, and filtering process. The approach is significant to isolate the stray light, to measure the photocurrent at the frequency of interest and minimize the noise due to dark current.

While photons are emitted in all direction, and only a small fraction is anticipated to arrive at the device under test due to the low view factors, the predicted fraction of power irradiance arriving at the detector from the blackbody is illustrated in Fig. 1. The size area of metallic aperture (3.14×10^{-4} m^2) positioned in front of the blackbody is one-quarter of the size area of blackbody window (1.256×10^{-3} m^2), predicting a 0.25 of power irradiance transmission. Collimating lens and bandpass filter are placed optimally based on the optical characteristic of those components, the optical path propagates through the CaF_2 collimating lens (4.91×10^{-4} m^2) positioned 10 cm after the aperture and bandpass filter (4.91×10^{-4} m^2) aligned at a 10 cm distance after the collimating lens. The transmittance ratio of CaF_2 collimating lens and bandpass filters were included in the mathematical solver. Considering that the CaF_2 collimating lens and bandpass filters size area are bigger than the metallic aperture, only the transmission losses are considered at the lens and bandpass filters. Therefore, it is reasonably assumed that the coupling losses are negligible. Lastly, the devices under test area were in the range of ($1–7.07 \times 10^{-6}$ m^2), a reasonable loss of power irradiance is predicted in the range of 0.02–0.014, taking into account the ratio of the size area of the incoming light beam to the area of the photodetector. With reference to the overall system, the power irradiance landing on the photodetectors is estimated to fall in the range of 0.05–0.36 % with reference to the incoming power irradiance from blackbody source.

The photon emitted from the blackbody radiation was collimated by the aperture and CaF_2 lens, passing through the chopper before landing on the device under test. The photocurrent of photodetectors, $I_{ph1}(\lambda)$ as a result of the exposure to the blackbody radiation was measured with the lock-in amplifier. The radiation power impinging onto the photodetectors is calculated with reference to the photocurrent density measurement and responsivity information using Eq. (2) -(3).

$$I_{ph1}\left(\frac{A}{m^2}\right)(\lambda) = R\left(\frac{A}{W}\right)(\lambda) * nm \times P\left(\frac{\frac{W}{m^2}}{nm}\right)(\lambda) \tag{2}$$

$$I_{ph1}(\lambda) = R_1\, P_{1,act}(\lambda) + R_2\, P_{2,act}(\lambda) + R_3\, P_{3,act}(\lambda) + \ldots\ldots + R_n\, P_{n,act}(\lambda) \tag{3}$$

where $P_{1,act}(\lambda)$, $P_{2,act}(\lambda)$, $P_{3,act}(\lambda)$, … $P_{n,act}(\lambda)$ are the actual power irradiance landing on the devices under test. Meanwhile, R_1, R_2, R_3 … R_n are the responsivity information with respect to the wavelength, extracted from the datasheet of the commercial devices. The responsivity information is tabulated from the datasheet in a small step size of 10 nm to ensure accurate mathematical results. The ideal power irradiance of blackbody source, $P_{i,ideal}(\lambda)$ with respect to the wavelength of operation and blackbody temperature was then solved using Planck's law [39]. As shown in Eq. (4), in reference to the actual power landing on the device under test, the power irradiance based on the ideal blackbody irradiance are expressed in the form of ratio with respect to the $P_{1,ideal}(\lambda)$ at the initial wavelength of reference. The prediction of the power density impinging on the device under test is solved considering the photocurrent density, responsivity, and ratio power information. Using Eq. (5), $P_{1,act}(\lambda)$ is calculated based on the photocurrent, $Ratio(\lambda)$ and responsivity, R information. As shown in Eq. (6), the $Ratio(\lambda)$ in Eq. (5) is expressed as the power ratio and responsivity information with reference to the step size of wavelength. Eq. (7) illustrates the detail expression of power ratio and responsivity information across the given range of wavelength. The information of $P_{1,act}(\lambda)$ solved in Eq. (5) will then be substituted into Eq. (4) to solve for the $P_{2,act}(\lambda)$, $P_{3,act}(\lambda)$, … and $P_{4,act}(\lambda)$ in Eq. (3), accordingly.

$$I_{ph1}(\lambda) = R_1\, P_{1,act}(\lambda) + R_2\frac{P_{2,ideal}(\lambda)}{P_{1,ideal}(\lambda)}P_{1,act}(\lambda) + R_3\frac{P_{3,ideal}(\lambda)}{P_{1,ideal}(\lambda)}\, P_{1,act}(\lambda) + \ldots\ldots + R_n\frac{P_{n,ideal}(\lambda)}{P_{1,ideal}(\lambda)}P_{1,act}(\lambda) \tag{4}$$

$$I_{ph1}(\lambda) = P_{1,act}(\lambda)(R_1 + Ratio(\lambda)) \tag{5}$$

$$Ratio(\lambda) = \sum_{i=2}^{n}\frac{P_{i,ideal}(\lambda)}{P_{1,ideal}(\lambda)}R_i \tag{6}$$

$$Ratio(\lambda) = \frac{P_{2,ideal}(\lambda)}{P_{1,ideal}(\lambda)}R_2 + \frac{P_{3,ideal}(\lambda)}{P_{1,ideal}(\lambda)}R_3 + \ldots\ldots + \frac{P_{n,ideal}(\lambda)}{P_{1,ideal}(\lambda)}R_n \tag{7}$$

Nevertheless, to portray the actual spectral irradiance scenario, the photocurrent measurement of photodetectors, $I_{ph2}\ (\lambda)$ is solved taking into consideration the transmission property of Alumina radiator. In addition, the optical transmission property of CaF_2 collimating lens was incorporated into the mathematical model, as shown in Eq. (8).

$$I_{ph2}\left(\frac{A}{m^2}\right)(\lambda) = \text{Alumina radiator} \times CaF_2 \times R\left(\frac{A}{W}\right)(\lambda) * nm \times P\left(\frac{\frac{W}{m^2}}{nm}\right)(\lambda) \tag{8}$$

where the transmission ratio of alumina radiator is taken as a constant value of 0.9 (90 % transmission) with respect to the wavelength from the datasheet [45]. With reference to Fig. 1, the data was taken in the average of three measurements with 2–4% of standard deviation, considering the possibility of experimental or measurement error. Meanwhile, the transmission ratio of CaF_2 collimating lens was extracted from the datasheet with a 10 nm step size [46], matching the 10 nm step size of the responsivity information from the device datasheet. At the validation stage with bandpass filters, the calculation step size was narrowed down to 1 nm to portray a better overlapping range for the validation procedure. Using Eq. (7), the power impinging onto the devices, as listed in Table 1, was solved in accordance with their operational wavelength.

To further verify and validate the trend of spectral irradiances solved in Eq. (8), the power density calculation was then focused on the narrow range of wavelength using the 1000 nm, 1400 nm, 1500 nm and 2000 nm bandpass filters. For the photocurrent measurement with the consideration of the optical transmission of the bandpass filter, $I_{ph3}(\lambda)$, the transmission ratio of bandpass filters from the datasheet was included as in Eq. (9) with a 1 nm wavelength step size. A small step size of 1 nm is considered in the mathematical calculation to give a more accurate result, as the bandpass filters have a narrower operating wavelength range (50 nm).

$$I_{ph3}\left(\frac{A}{m^2}\right)(\lambda) = \text{Alumina radiator} \times CaF_2 \times \text{Bandpass Filter} \times R\left(\frac{A}{W}\right)(\lambda) * nm \times P\left(\frac{\frac{W}{m^2}}{nm}\right)(\lambda) \tag{9}$$

Based on Eq. (9), the power density was solved in the bandpass filter's wavelength range. The data is compared with the spectral irradiance solved in Eq. (8) at the respective wavelengths, to validate the capability of predictive analysis for power spectral irradiance in NIR (400 nm–2600 nm) using a single pixel detector.

3. Results and discussion

The power density spectrum of single-pixel photodetectors (Si, Ge, $In_{0.53}Ga_{0.47}As$, $In_{0.73}Ga_{0.27}As$, and $In_{0.83}Ga_{0.17}As$) is firstly solved using Eq. (8) under 1000 °C and 1500 °C blackbody temperature, taking into consideration factors such as alumina radiator, collimating lens, responsivity of photodetector and the power density ratio with reference to the ideal blackbody source. The collected power density information solved using Eq. (8) maps across the wavelength range of 400 nm–2600 nm with 10 nm step size, providing spectrum coverage for the NIR wavelength region. As illustrated in Fig. 2 (a) and (b), Si photodetector portrays the power density information in the shorter wavelength region 400–1100 nm. Si photodetector provides coverage of power density information in the shorter wavelength range 400–800 nm, which was not covered by other devices. On the other hand, Ge and $In_{0.53}Ga_{0.47}As$ demonstrate the power density information in the spectrum range of 800–1800 nm. The power density in the range of 900–2160 nm is then solved

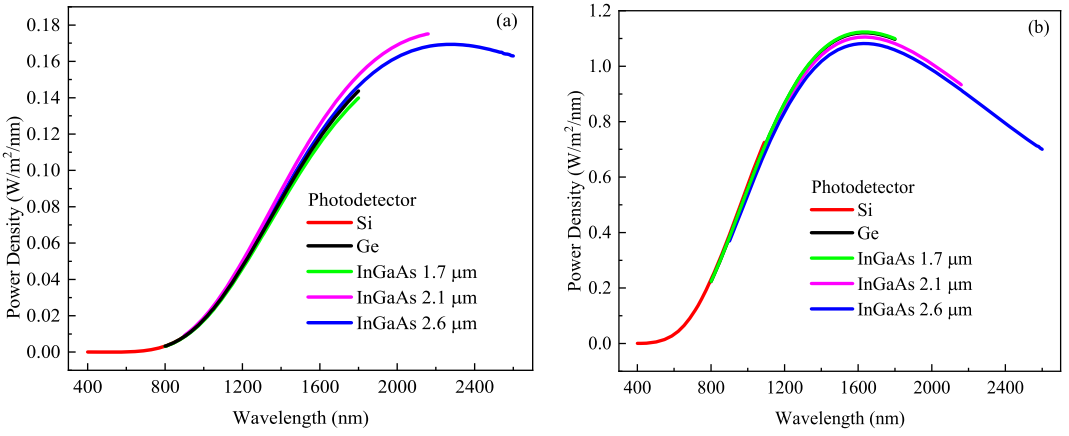

Fig. 2. (a) Power density spectrum of photodetectors for 1000 °C. (b) Power density spectrum of photodetectors for 1500 °C blackbody temperature.

with the $In_{0.73}Ga_{0.27}As$ photodetector, extending the wavelength tail from 1800 nm up to 2160 nm. The overlapping in power density spectrum for Ge, $In_{0.53}Ga_{0.47}As$ and $In_{0.73}Ga_{0.27}As$ photodetectors confirm the consistency in power spectrum result for 800–1100 nm, demonstrating a tolerable range of percentage error in solving the power density using single device. Meanwhile, $In_{0.83}Ga_{0.17}As$ covers the power density information in the range of 900–2600 nm. $In_{0.83}Ga_{0.17}As$ photodetector maps the information range up to 2600 nm, giving the needed information on the power density at the NIR wavelength tail region. The power density of devices under test depicts a good fit with each other, reporting 0 %–4.9 % percentage differences between the calculated power densities from different photodetectors for 1000 °C as shown in Figs. 2 (a), and 0 %–3.1 % percentage differences for 1500 °C in Fig. 2 (b). Under different measured radiation temperatures, the consistency in the power spectrum density result from the five commercial photodetectors give assurance in the practicality of single pixel device as the power density estimation indicator.

With reference to the power density spectrum as presented in Fig. 2, the incident power density on the photodetectors were calculated based on the integration of area under the graph and plotted in Fig. 3. The percentage of radiation power on the devices under test with respect to the power from blackbody source is then calculated, considering 100 % of the blackbody beam spectrum intensity. The highest percentage of radiation power on the photodetectors was 0.389 %, measured under 1500 °C using the $In_{0.83}Ga_{0.17}As$ photodetector, which is equivalent to 1459 W/m^2 power density landing on the device. On the contrary, the lowest percentage of radiation power landing on the Si photodetector is reported to be 0.0063 % with 4.189 W/m^2 of power at 1000 °C. The calculated power irradiances fall within the range of the predicted power landing on the photodetectors as discussed in Fig. 1. The difference in the percentage of radiation power is due to the thermal degradation from the radiator to the device under test, which is mainly contributed by factors such as distance of the measured device from radiator and heat lost to the surrounding [47]. A few other possible influencing factors were the range of tolerance in the transmittance of optical lenses and slight deviation in the responsivity from the actual values of the photodiodes used in the measurement. Research by Wojtczuk et al. [48] has reported 0.3 % of blackbody incidence on the $In_{0.62}Ga_{0.38}As$ cell, which is located 7.3 cm from the 1000 °C blackbody source aperture. Nevertheless, the efficiency calculation method was not clearly indicated in the research. To improve the TPV system efficiency, radiation recirculation method such as back surface reflector and parabolic reflector were proposed to recycle the phonons [49]. It is also worth noting that the information of radiation power density on photodetector is significant to solve for the accurate PV/TPV cell and system efficiency parameters [50].

Validation of power density behaviour across the wavelength spectrum was carried out with reference to Eq. (9). Bandpass filters were integrated in the setup to mainly measure the spectrum in the range between 975 nm–1025 nm (1000 BP), 1375 nm–1425 nm

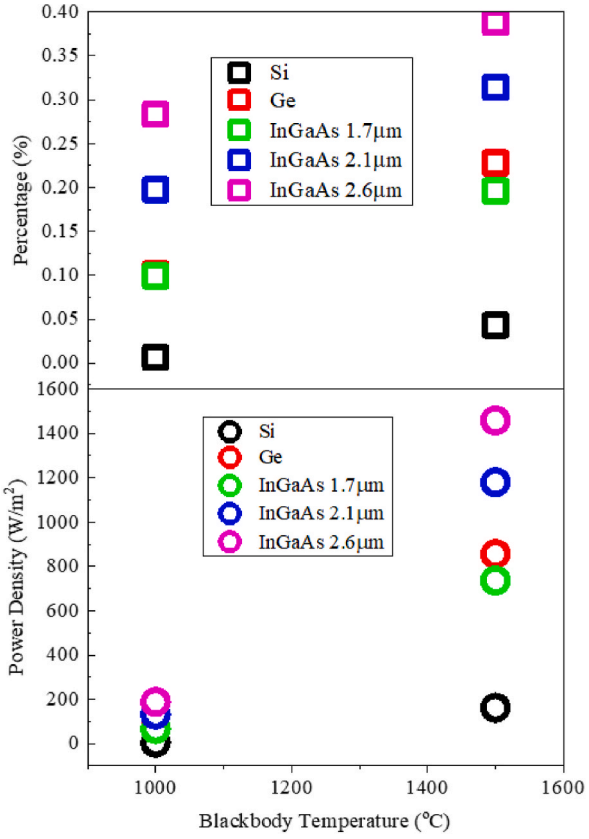

Fig. 3. Percentage of radiation power on the photodetectors (assuming 100 % blackbody beam intensity) and power density of devices under 1000 °C and 1500 °C blackbody temperature.

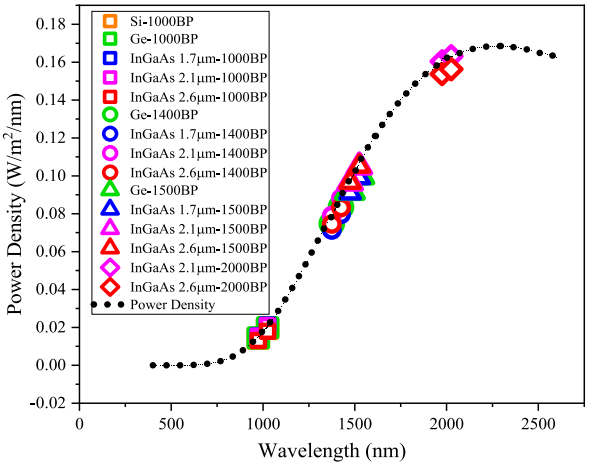

Fig. 4. Validation of power densities with bandpass filters for 1000 °*C* blackbody temperature. *(The power density data with bandpass filter is calculated with a 2 nm step size, but for clarity purpose, only 2–3 data points are plotted.).

(1400 BP), 1475 nm–1525 nm (1500 BP), and 1975 nm–2025 nm (2000 BP) with 1 nm step size while filtering other wavelengths. This filtration process narrows down the wavelength of study, focusing on the power density information at specific wavelengths of interest whilst reducing the error of calculation such as transmission ratio of CaF_2 collimating lens and responsivity ratio with respect to wavelength. The spectrum of Si photodetector was validated with 1000 BP, while Ge and $In_{0.53}Ga_{0.47}As$, which share similar wavelength range (800–1100 nm), were validated with 1000 BP, 1400 BP, and 1500 BP filters. Meanwhile, $In_{0.73}Ga_{0.27}As$ and $In_{0.83}Ga_{0.17}As$ were validated with 1000 BP, 1400 BP, 1500 BP and 2000 BP filters due to the longer wavelength coverage. An additional 2000 nm bandpass filter was considered to map the power density of the two photodetectors at the wavelength tail of $In_{0.73}Ga_{0.27}As$ and $In_{0.83}Ga_{0.17}As$, notably the selection of bandpass filter was based on the wavelength range of device.

Figs. 4 and 5 present the validation result using bandpass filters under 1000 °C and 1500 °C blackbody radiation, respectively. The power density graph for direct measurement setup was taken based on the average data of power density information from Fig. 2 (a) and (b). The deviation error of the validation result of bandpass filters with respect to the power density measurement in Figs. 4 and 5 were calculated and listed in Table 2. For Si photodetector, validation result shows that the 1000 nm bandpass filter shows good agreement compared to direct measurement, recording a 6.69 % and 2.5 % deviation for 1000 °C and 1500 °C, respectively. Next for the Ge photodetector, results from the bandpass filters record a difference of 0.098 %–5.51 % in the power density for the 1000 °C and 1.7 %–4.25 % for 1500 °C blackbody temperature. Moving on to the $In_{0.53}Ga_{0.47}As$ photodetector, the bandpass filters data fitted well with power density data with a percentage difference range of 3.98 %–7.45 % under 1000 °C and 0.29 %–1.81 % under 1500 °C blackbody temperature. The slight deviation in result is possibly due to the systematic experimental errors such as loss of information across the filtration of bandpass filter, aliasing and also signal leakage [51]. This could be further improved by having a direct near field measurement setup, eliminating possible loss of information. As shown in Fig. 5, validation from bandpass filters show decent

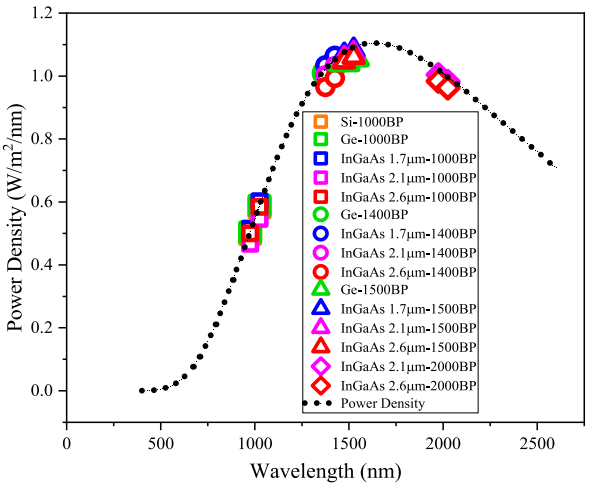

Fig. 5. Validation of power densities with bandpass filters for 1500 °*C* blackbody temperature. *(The power density data with bandpass filter is calculated with a 2 nm step size, but for clarity purpose, only 2–3 data points are plotted.).

Table 2
of deviation for validation of power densities with bandpass filters.

Percentage of Deviation under 1000 °C Blackbody Temperature (%)					
	Si	Ge	$In_{0.53}Ga_{0.47}As$	$In_{0.73}Ga_{0.27}As$	$In_{0.83}Ga_{0.17}As$
1000 BP	6.69	4.46	4.91	0.378	7.89
1400 BP	–	5.51	7.45	2.11	7.22
1500 BP	–	0.098	3.98	2.94	2.62
2000 BP	–	–	–	0.304	4.45
Percentage of Deviation under 1500 °C Blackbody Temperature (%)					
	Si	Ge	$In_{0.53}Ga_{0.47}As$	$In_{0.73}Ga_{0.27}As$	$In_{0.83}Ga_{0.17}As$
1000 BP	2.5	1.8	0.29	7.66	0.50
1400 BP	–	1.7	1.58	2.03	3.63
1500 BP	–	4.25	1.81	2.46	2.86
2000 BP	–	–	–	1.49	2.42

data fitting for $In_{0.73}Ga_{0.27}As$ with a range of 0.304 %–7.66 % power density under 1000 °C and 1500 °C blackbody temperatures. The power irradiance passing through the bandpass filters for $In_{0.83}Ga_{0.17}As$ agrees well with the direct measurement recording a difference range of 2.62 %–7.89 % under 1000 °C and 0.5 %–3.63 % under 1500 °C blackbody temperatures, as illustrated in Table 2.

The validation of power densities with bandpass filters gives a good confidence of the power density spectrum solver using single pixel detector, reporting <7.89 % and <7.66 % of deviation error for 1000 °C and 1500 °C, respectively. The proposed method is a simpler, cost-effective, and agile way of solving the power density from blackbody landing on photodetectors, which could be useful in solving the PV/TPV cell and system efficiency accurately. In comparison with the other measurement and simulation methods reviewed in the introduction section, the proposed single-pixel detector method solves for the actual power landing on the device across a broader wavelength spectrum (up to 2600 nm) with an acceptable range of tolerance. Moreover, the power spectrum irradiances need to be validated with bandpass filters, to give better confidence in the result. One major limitation of the power irradiance measurement using single pixel-detector would be that some assumptions need to be carefully taken into consideration in the power density solver, for example the emissivity information of blackbody emitter, transmission spectra of collimating lens, together with the transmission spectrum information of bandpass filters. As compared to other equipment such as spectrophotometer, one constraint of the proposed method is that it requires signal modulation to modulate the incoming photons at a certain frequency. However, this proposed method could be further developed into a commercial portable and cost-effective spectrum irradiance analyser, which can be integrated into other spectral irradiance measurement applications such as photodetectors, PV cell design, and security applications.

4. Conclusion

This work demonstrates a newly derived predictive mathematical method to determine the power density irradiances of blackbody sources at 1000 °C and 1500 °C using the Si, Ge, $In_{0.53}Ga_{0.47}As$, $In_{0.73}Ga_{0.27}As$ and $In_{0.83}Ga_{0.17}As$ photodetectors. Based on the measured photocurrent information and predictive mathematical model, the spectral irradiance of photodetector was determined with a percentage difference <4.9 %, presenting an accurate spectrum estimation at a wide range of radiation temperatures. To confirm and validate the power irradiance measurement at a narrow wavelength, bandpass filters were used to solve for the power irradiance information at a specific wavelength range, recording <7.89 % deviation error. To conclude, these findings could be further made useful to develop a cost-effective method of measuring and determining the spectrum irradiances of different objects at various range of blackbody temperatures. The proposed solver using single pixel detector simplifies the irradiance data extraction procedure without resorting to complex optoelectronic sensors and gratings. This agile method can be further developed into a commercial portable and cost-effective spectrum irradiance analyser, which can be integrated with multiple applications such as photovoltaic and thermophotovoltaic power harvesting usage, medical imaging, safety, and security applications.

Author contribution statement

Hui Jing Lee: Performed the experiments; Analysed and interpreted the data; Wrote the paper.
Pin Jern Ker: Conceived and designed the experiments.
Mansur Mohammed Ali Gamel, Md. Zaini Jamaludin, Yew Hoong Wong: Analysed and interpreted the data; Contributed reagents, materials, analysis tools or data.

Data availability statement

The data will be made available upon request.

Declaration of competing interest

The authors declare that they have no known competing financial interests or personal relationships that could have appeared to

influence the work reported in this paper.

Acknowledgments

This work was supported by Tenaga Nasional Berhad (TNB) and UNITEN through the BOLD Refresh Publication Fund under the project code of J510050002-IC-6 BOLDREFRESH2025-Centre of Excellence, and BOLD Research Grant under the project code of J510050002/2023051.

References

[1] R.J. Matson, K.A. Emery, R.E. Bird, Terrestrial solar spectra, solar simulation and solar cell short-circuit current calibration: a review, Sol. Cell. 11 (2) (1984) 105–145, https://doi.org/10.1016/0379-6787(84)90022-X. Mar.
[2] A.V. Parisi, D. Igoe, N.J. Downs, J. Turner, A. Amar, M.A.A. Jebar, Satellite monitoring of environmental solar ultraviolet a (Uva) exposure and irradiance: a review of omi and gome-2, Rem. Sens. 13 (4) (2021) 1–19, https://doi.org/10.3390/rs13040752.
[3] I. Ermolli, K. Matthes, T. Dudok de Wit, N.A. Krivova, K. Tourpali, M. Weber, Y.C. Unruh, L. Gray, U. Langematz, P. Pilewskie, E. Rozanov, W. Schmutz, A. Shapiro, S.K. Solanki, T.N. Woods, Recent variability of the solar spectral irradiance and its impact on climate modelling, Atmos. Chem. Phys. 13 (8) (2013) 3945–3977, https://doi.org/10.5194/acp-13-3945-2013. Apr.
[4] H. Wu, Z. Zhou, S. Shan, Optimal design principle of a cascading solar photovoltaic system with concentrating spectrum splitting and reshaping, Renew. Energy 197 (June) (Sep. 2022) 197–210, https://doi.org/10.1016/j.renene.2022.07.129.
[5] C. Chang, H.H. Cheng, G.A. Sevison, J.R. Hendrickson, Z. Li, I. Agha, J. Mathews, R.A. Soref, G. Sun, Power-dependent investigation of photo-response from GeSn-based p-i-n photodetector operating at high power density, Materials 15 (3) (2022), https://doi.org/10.3390/ma15030989.
[6] T.W. Kim, S. Hyun, K. Jae, W. Shim, D. Kyung, Organic photodiode with dual functions of indoor photovoltaic and high – speed photodetector, Front. Optoelectron. (–7) (2022) 1, https://doi.org/10.1007/s12200-022-00024-5.
[7] M. Fligge, S.K. Solanki, The solar spectral irradiance since 1700, Geophys. Res. Lett. 27 (14) (Jul. 2000) 2157–2160, https://doi.org/10.1029/2000GL000067.
[8] E.J. Tervo, R.M. France, D.J. Friedman, M.K. Arulanandam, R.R. King, T.C. Narayan, C. Luciano, D.P. Nizamian, B.A. Johnson, A.R. Young, L.Y. Kuritzky, E. E. Perl, M. Limpinsel, B.M. Kayes, A.J. Ponec, D.M. Bierman, J.A. Briggs, M.A. Steiner, Efficient and scalable GaInAs thermophotovoltaic devices, Joule 6 (11) (Nov. 2022) 2566–2584, https://doi.org/10.1016/j.joule.2022.10.002.
[9] A.W. Schmalwieser, S. Eschenbacher, J. Schreder, UV-Biometer - the usage of erythemal weighted broadband meters for other biological effects, J. Photochem. Photobiol. B Biol. 230 (February) (2022), 112442, https://doi.org/10.1016/j.jphotobiol.2022.112442.
[10] B.Y. Kim, K.T. Lee, I.S. Zo, S.H. Lee, H.S. Jung, S.H. Rim, J.P. Jang, Calibration of the pyranometer sensitivity using the integrating sphere, Asia-Pacific J. Atmos. Sci. 54 (4) (2018) 639–648, https://doi.org/10.1007/s13143-018-0085-0.
[11] V. Salgueiro, M.J. Costa, J.L. Guerrero-Rascado, F.T. Couto, D. Bortoli, Characterization of forest fire and Saharan desert dust aerosols over south-western Europe using a multi-wavelength Raman lidar and Sun-photometer, Atmos. Environ. 252 (March) (2021), https://doi.org/10.1016/j.atmosenv.2021.118346.
[12] J.L. Balenzategui, M. Molero, J.P. Silva, F. Fabero, J. Cuenca, E. Mejuto, J. De Lucas, Uncertainty in the calibration transfer of solar irradiance scale: from absolute cavity radiometers to standard pyrheliometers, Solar 2 (2) (Apr. 2022) 158–185, https://doi.org/10.3390/solar2020010.
[13] S. Yuan, D. Naveh, K. Watanabe, T. Taniguchi, F. Xia, A wavelength-scale black phosphorus spectrometer, Nat. Photonics 15 (8) (2021) 601–607, https://doi.org/10.1038/s41566-021-00787-x.
[14] D. Meloni, C. Di Biagio, A. Di Sarra, F. Monteleone, G. Pace, D.M. Sferlazzo, Accounting for the solar radiation influence on downward longwave irradiance measurements by pyrgeometers, J. Atmos. Ocean. Technol. 29 (11) (2012) 1629–1643, https://doi.org/10.1175/JTECH-D-11-00216.1.
[15] J. Kammerer, S.P. Quanz, F. Dannert, Large interferometer for exoplanets (LIFE), Astron. Astrophys. 668 (2022) A52, https://doi.org/10.1051/0004-6361/202243846.
[16] J.U. Morley, L.J.B. Mcarthur, D. Halliwell, Y. Poissant, S. Pelland, CCD fiber optic spectrometer for the measurement of spectral irradiance, Reliab. Photovolt. Cells, Modul. Components, Syst. III 7773 (2010) 1–12, https://doi.org/10.1117/12.860872.
[17] E.V. Kuvaldİn, A.A. Shulga, Combined method of energy and power meters calibration in optical range, Acta Mater. Turc. 4 (July) (2020) 1–7.
[18] E.M. El-Mahdy, S.A. El-Mongy, A.M. Karmalawi, Apparatus for calibration of photovoltaic cells at national institute of standards, IEEE Instrum. Meas. Mag. 25 (3) (2022) 22–29, https://doi.org/10.1109/MIM.2022.9759359.
[19] T. Pohl, P. Meindl, J. Hollandt, U. Johannsen, L. Werner, Particularities of pyroelectric detectors in absolute measurements of chopped radiation shown for the example of a spectral responsivity calibration in the near-and mid-infrared spectral range at two primary radiometric standards, J. Sensors Sens. Syst. 11 (1) (2022) 61–73, https://doi.org/10.5194/jsss-11-61-2022.
[20] X. Huang, A.N. Chalmers, Review of wearable and portable sensors for monitoring personal solar UV exposure, Ann. Biomed. Eng. 49 (3) (2021) 964–978, https://doi.org/10.1007/s10439-020-02710-x.
[21] Y. Cui, L. Hong, T. Zhang, H. Meng, H. Yan, Accurate photovoltaic measurement of organic cells for indoor applications ll Commentary, Joule 5 (5) (2021) 1016–1023, https://doi.org/10.1016/j.joule.2021.03.029.
[22] J. Bendig, D. Gautam, Z. Malenovsky, A. Lucieer, Influence of cosine corrector and uas platform dynamics on airborne spectral irradiance measurements, in: IGARSS 2018 - 2018 IEEE International Geoscience and Remote Sensing Symposium, 2018, pp. 8822–8825, https://doi.org/10.1109/IGARSS.2018.8518864. Jul.
[23] A. Ravindran, D. Nirmal, B.K. Binola, J. Ajayan, P. Prajoon, Investigation on impact of GaAs and GaN blazed grating for high performance UV-VIS spectrometer, 3rd Int. Conf. Electron. Sustain. Commun. Syst. ICESC 2022 - Proc., no. Icesc (2022) 1326–1332, https://doi.org/10.1109/ICESC54411.2022.9885635.
[24] A. Ravindran, D. Nirmal, B.K. Binola, K.P. Pinkymol, P. Prajoon, J. Ajayan, InGaAs based gratings for UV–VIS spectrometer in prospective mRNA vaccine research, Opt. Quantum Electron. 54 (9) (2022) 1–15, https://doi.org/10.1007/s11082-022-04002-1.
[25] M.R.M. Atalla, S. Assali, S. Koelling, A. Attiaoui, O. Moutanabbir, High-bandwidth extended-SWIR GeSn photodetectors on Silicon achieving ultrafast broadband spectroscopic response, ACS Photonics 9 (4) (Apr. 2022) 1425–1433, https://doi.org/10.1021/acsphotonics.2c00260.
[26] E. Catelli, G. Sciutto, S. Prati, M.V. Chavez Lozano, L. Gatti, F. Lugli, S. Silvestrini, S. Benazzi, E. Genorini, R. Mazzeo, A new miniaturised short-wave infrared (SWIR) spectrometer for on-site cultural heritage investigations, Talanta 218 (March) (2020), 121112, https://doi.org/10.1016/j.talanta.2020.121112.
[27] M.M.A. Gamel, H.J. Lee, W.E.S.W.A. Rashid, P.J. Ker, L.K. Yau, M.A. Hannan, M.Z. Jamaludin, A review on thermophotovoltaic cell and its applications in energy conversion: issues and recommendations, Materials 14 (17) (2021) 4944, https://doi.org/10.3390/ma14174944. Aug.
[28] M.M.A. Gamel, P.J. Ker, W.E.S.W.A. Rashid, H.J. Lee, M.A. Hannan, M.Z. Jamaludin, Performance of Ge and In0.53Ga0.47As thermophotovoltaic cells under different spectral irradiances, IEEE Access 9 (2021) 37091–37102, https://doi.org/10.1109/ACCESS.2021.3062075.
[29] E. López, I. Artacho, A. Datas, Thermophotovoltaic conversion efficiency measurement at high view factors, Sol. Energy Mater. Sol. Cells 250 (September 2022) (2023), 112069, https://doi.org/10.1016/j.solmat.2022.112069. Jan.
[30] C. Lucchesi, D. Cakiroglu, J.P. Perez, T. Taliercio, E. Tournié, P.O. Chapuis, R. Vaillon, Near-field thermophotovoltaic conversion with high electrical power density and cell efficiency above 14, Nano Lett. 21 (11) (2021) 4524–4529, https://doi.org/10.1021/acs.nanolett.0c04847.
[31] E. Rousseau, A. Siria, G. Jourdan, S. Volz, F. Comin, J. Chevrier, J.J. Greffet, Radiative heat transfer at the nanoscale, Nat. Photonics 3 (9) (2009) 514–517, https://doi.org/10.1038/nphoton.2009.144.
[32] S. Shen, A. Narayanaswamy, G. Chen, Surface phonon polaritons mediated energy transfer between nanoscale gaps, Nano Lett. 9 (8) (2009) 2909–2913, https://doi.org/10.1021/nl901208v.

[33] M. Gamel, P.J. Ker, H.J. Lee, W.E.S.W.A. Rashid, M.A. Hannan, J. David, M.Z. Jamaludin, Multi-dimensional optimization of In0.53Ga0.47As thermophotovoltaic cell using real coded genetic algorithm, Nat. Sci. Rep. (2021), https://doi.org/10.21203/rs.3.rs-111565/v1.
[34] M. Tan, L. Ji, Y. Wu, P. Dai, Q. Wang, K. Li, T. Yu, Y. Yu, S. Lu, H. Yang, Investigation of InGaAs thermophotovoltaic cells under blackbody radiation, Appl. Phys. Express 7 (9) (2014) 4–7, https://doi.org/10.7567/APEX.7.096601.
[35] P.A. Iles, C. Chu, E. Linder, The influence of bandgap on TPV converter efficiency, AIP Conf. Proc. 358 (1996) 446–457, https://doi.org/10.1063/1.49705.
[36] C. Gaber, M. Demuth, C. Schluckner, C. Hochenauer, Thermochemical analysis and experimental investigation of a recuperative waste heat recovery system for the tri-reforming of light oil, Energy Convers. Manag. 195 (March) (2019) 302–312, https://doi.org/10.1016/j.enconman.2019.04.086.
[37] R. Pili, L. García Martínez, C. Wieland, H. Spliethoff, Techno-economic potential of waste heat recovery from German energy-intensive industry with Organic Rankine Cycle technology, Renew. Sustain. Energy Rev. 134 (February) (2020), 110324, https://doi.org/10.1016/j.rser.2020.110324.
[38] Y. Zhang, Q. Li, H. Zhou, Theoretical Foundation and Basic Properties of Thermal Radiation, 2016, https://doi.org/10.1016/b978-0-12-800966-6.00001-6.
[39] J.C. Cuevas, Thermal radiation from subwavelength objects and the violation of Planck's law, Nat. Commun. 10 (1) (2019) 1–4, https://doi.org/10.1038/s41467-019-11287-6.
[40] S. Elements, "High Speed Detectors (BPX65) Series BPX Spectral Response Graph Capacitance versus Bias Voltage.".
[41] Thorlabs, Photodiodes Cation Sheet, 2011.
[42] OSIOptoelectronics, FCI-InGaAs-XXX-X FCI-InGaAs-XXX-X (2020) 88–89.
[43] Hamamatsu, InGaAs PIN photodiodes G12182 4 (2020) 1–8.
[44] Hamamatsu, InGaAs PIN photodiodes G12183 5 (2020) 1–8.
[45] N. Avci, J. Musschoot, P.F. Smet, K. Korthout, A. Avci, C. Detavernier, D. Poelman, Microencapsulation of moisture-sensitive CaS:Eu[2+] particles with aluminum oxide, J. Electrochem. Soc. 156 (11) (2009) J333, https://doi.org/10.1149/1.3211959.
[46] Calcium Fluoride Plano Convex (PCX) Lenses, 2014, 74657.
[47] V.P. Khvostikov, Y.V. Grachev, A.S. Vlasov, O.A. Khvostikova, S.V. Sorokina, Reducing optical losses in thermophotovoltaic systems, J. Power Sources 501 (March) (2021), 229972, https://doi.org/10.1016/j.jpowsour.2021.229972.
[48] S. Wojtczuk, E. Gagnon, L. Geoffroy, T. Parodos, InxGa1−xAs thermophotovoltaic cell performance vs bandgap, AIP Conference Proceedings, 1995 321 (1995) 177–187, https://doi.org/10.1063/1.47020.
[49] D. Feng, S.K. Yee, Z.M. Zhang, Improved performance of a near-field thermophotovoltaic device by a back gapped reflector, Sol. Energy Mater. Sol. Cells 237 (June 2021) (2022), 111562, https://doi.org/10.1016/j.solmat.2021.111562.
[50] T. Inoue, K. Ikeda, B. Song, T. Suzuki, K. Ishino, T. Asano, S. Noda, Integrated near-field thermophotovoltaic device overcoming blackbody limit, ACS Photonics 8 (8) (2021) 2466–2472, https://doi.org/10.1021/acsphotonics.1c00698.
[51] C.A. Mack, Systematic errors in the measurement of power spectral density, J. Micro/Nanolithography, MEMS, MOEMS 12 (3) (2013), 033016, https://doi.org/10.1117/1.JMM.12.3.033016.